OPTIMIZING THE DESIGN OF FT-IR SPECTROSCOPIC IMAGING INSTRUMENTS TO OBTAIN INCREASED SPATIAL RESOLUTION OF CHEMICAL SPECIES

R. Reddy[12], *D. Mayerich*[2], *M. Walsh*[2], *M. Schulmerich*[12], *P. S. Carney*[23], *R. Bhargava*[12345]

[1]Department of Bioengineering, University of Illinois at Urbana-Champaign (UIUC)
[2]Beckman Institute for Advanced Science and Technology, UIUC
[3]Department of Electrical and Computer Engineering, UIUC
[4]Department of Mechanical Engineering, Micro and Nanotechnology Laboratory, UIUC
[5]University of Illinois Cancer Center

ABSTRACT

Fourier transform infrared (FT-IR) spectroscopic imaging provides spatially resolved chemical information. Recent developments have shown that this chemical information can be used to determine tissue cell types. Our goal is then to use the spatial distribution of tissue cell types to perform accurate diagnosis of cancer. However, this step is limited by the spatial resolution provided by current imaging systems. In this paper, we demonstrate that these instruments can be designed to provide better spatial resolution for tissue chemistry. We present an optical model for the propagation of light through an FT-IR spectroscopic imaging system. Using this model, we minimally modify an existing FT-IR spectroscopic imaging system to obtain significantly higher resolution and image quality. We demonstrate that it is possible to identify previously obscured tissue types by performing histological classification based on bio-chemically derived spectral features (metrics).

1. INTRODUCTION

Mid-infrared spectroscopy has been used extensively for the identification and quantification of chemical composition of specimens.[1] When mid-infrared light is incident on a specimen, the vibrational modes of constituent molecules resonate with light of certain frequencies. A pattern of absorption can be created in the entire mid-infrared frequency range by analyzing the response of the specimen. This pattern, called the absorbance spectrum, is characteristic of the chemical composition and contains information that helps distinguish chemically different specimens. It has been hypothesized that in human tissues, this information will allow us to determine the cell type and disease state of the tissue.

Combining mid-infrared spectroscopy with infrared microscopy has been a relatively recent development [2] and has led to the emergence of FT-IR spectroscopic imaging. However, commercially available imaging systems for the past decade do not fully utilize the optical capabilities of the instrument. We demonstrate this using an optical model for light propagation through an FT-IR spectroscopic imaging system. Moreover, we modify a current commercial instrument to implement the optimized design.

Finally, we demonstrate that it is possible to identify previously obscured chemical information using classification on these higher-resolution images. We perform cell-type classification using a two-class Bayesian model based on spectral features selected by experts and refined using a greedy approach. We then show that the improvement in resolution allows the identification of structural features important for cancer diagnosis in breast tumor biopsies.

2. THEORETICAL MODEL

A general model for FT-IR spectroscopic imaging is presented here. Different modeling paradigms of varying complexity are available for the analysis of optical instruments. Simple models based on ray (geometric) optics have been especially popular [3] for IR microscopy. Full-scale electromagnetic models are rigorous, but involve high computational load and complexity. It is prudent to choose the simplest model that incorporates all the phenomena of interest. We sought to understand the process of light propagation and image formation in an FT-IR spectroscopic imaging instrument. Hence, we forgo the full electromagnetic treatment [4] in favor of using the simpler scalar wave theory [5] framework.

2.1. System Equations

The system shown in Figure 1 can be analyzed using a modular approach by defining an operator for each component [6]. This approach provides a convenient means of modifying the analysis to accommodate any changes in the instrument. The relation between the field at the infrared source, $|U_S\rangle$, and the field just after the sample, $|U_j\rangle$, and the field at the detector ,

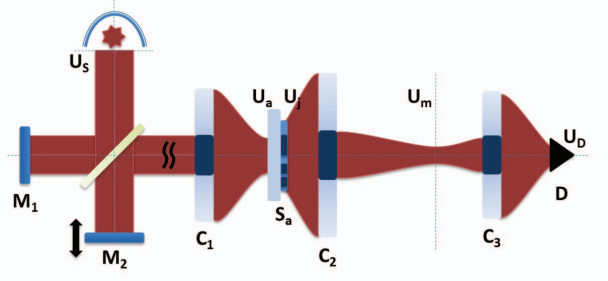


Fig. 1. Model for a FT-IR imaging system. The system consists of an interferometer coupled to a microscope system. Cassegrain C_1 focus light on to the sample S_a, C_2 and C_3 carry light from the sample to the detector D. The fields in different planes are also indicated.

$|U_D\rangle$, is given by the following equations.

$$|U_j\rangle = \mathbf{T}_S\mathbf{H}_{C_1}\mathbf{K}_{|d_{I-C1}|}\mathbf{I}_{\Delta_r}\mathbf{K}_{|d_{S-I}|}|U_S\rangle \quad (1)$$

$$|U_D\rangle = \mathbf{H}_{C_3}\mathbf{K}_{|d_{2-3}|}\mathbf{H}_{C_2}|U_j\rangle \quad (2)$$

$$= \mathbf{H}_{C_3}\mathbf{K}_{|d_{2-3}|}\mathbf{H}_{C_2}\mathbf{T}_S\mathbf{H}_{C_1}\mathbf{K}_{|d_{I-C1}|}\mathbf{I}_{\Delta_r}\mathbf{K}_{|d_{S-I}|}|U_S\rangle \quad (3)$$

where, $\mathbf{K}_{|d_{S-I}|}$ is the operator that propagates the field from the source to the beam-splitter, $\mathbf{I}_{\Delta_r}$ describes the propagation to and from the interferometer mirrors where Δ_r represents the difference in path-length caused by movement of M_2, $\mathbf{K}_{|d_{I-C1}|}$ corresponds to propagation from the beam-splitter to the cassegrain C_1, $\mathbf{H}_{C_1}$ describes the action of the cassegrain C_1 and $\mathbf{T}_S$ describes the interaction of the sample and incident light. $\mathbf{H}_{C_2}$ and $\mathbf{H}_{C_3}$ are the operator corresponding to the cassegrains C_2 and C_3 respectively. $\mathbf{K}_{|d_{2-3}|}$ corresponds to the propagation of the field between the two cassegrains. The kernels of these operators are described below.

$$\langle\mathbf{f}_2|\mathbf{K}_{|z|}|\mathbf{f}_1\rangle = \delta(\mathbf{f}_2-\mathbf{f}_1)e^{i2\pi\bar{\nu}\left(1-\frac{|\mathbf{f}_1|^2}{2\bar{\nu}^2}\right)|z|} \quad (4)$$

$$\langle\mathbf{f}_2|\mathbf{I}_{\Delta_r}|\mathbf{f}_1\rangle = \frac{1}{2}\delta(\mathbf{f}_2-\mathbf{f}_1)\left(1+e^{i4\pi\bar{\nu}\Delta_r}\right) \quad (5)$$

$$\langle\mathbf{f}_2|\mathbf{T}_S|\mathbf{f}_1\rangle = \tilde{t}(\mathbf{f}_2-\mathbf{f}_1) \quad (6)$$

$$\langle\mathbf{f}_2|\mathbf{H}_{C_i}|\mathbf{f}_1\rangle = \delta(\mathbf{f}_1+M_i\mathbf{f}_2)P(\mathbf{f}_1)Q^{\bar{\nu}M_i\mathrm{NA}_{C_i out}}_{\bar{\nu}M_i\mathrm{NA}_{C_i in}}(\mathbf{f}_1) \quad (7)$$

Here, $\mathbf{f}_i = (f_{xi}, f_{yi})$ are the x, y spatial frequencies and $\bar{\nu}$ is the wavenumber. The function $\tilde{t}$ is the Fourier transform of the transmission function [5], which defines the properties of light propagation through the material. M_i is the magnification corresponding to the cassegrain C_i. $\mathrm{NA}_{C_i in}$ and $\mathrm{NA}_{C_i out}$ correspond to the outer and inner numerical appertures of cassegrain C_i Functions P and Q are defined in eqs. 8 and 9. The function P captures the effect of far field propagation, expressing the physical fact that all spatial frequency components whose magnitude is larger than $\bar{\nu}$ result in exponentially decaying evanescent waves and do not propagate to the far field. The only propagating waves correspond to spatial frequencies retained by P.

$$P(\mathbf{f}) = \begin{cases} 1 & |\mathbf{f}| < \bar{\nu} \\ 0 & otherwise \end{cases} \quad (8)$$

A more general function Q is also defined that provides the transmitted frequencies of the cassegrain corresponding to its NA and central obscuration.

$$Q^b_a(\mathbf{f}) = \begin{cases} 1 & a < |\mathbf{f}| < b \\ 0 & otherwise \end{cases} \quad (9)$$

It may be noted that all the above operators are defined in the spatial frequency domain so as to facilitate analysis of spatial frequencies at every step.

Using these equations, the field incident on the sample, $\tilde{U}_a(\mathbf{f})$, is described in terms of the source and optical components as

$$\tilde{U}_a(\mathbf{f}) = Q^{\bar{\nu}\mathrm{NA}_{C_1 out}}_{\bar{\nu}\mathrm{NA}_{C_1 in}}(\mathbf{f})\tilde{U}_S(-M_{C_1}\mathbf{f})\left(1+e^{i4\pi\bar{\nu}\Delta_r}\right) \quad (10)$$

The field, $\tilde{U}_j(\mathbf{f})$, immediately after the sample is

$$\tilde{U}_j(\mathbf{f}) = \int d^2f^a\tilde{U}_a(\mathbf{f}^a)\tilde{t}(\mathbf{f}-\mathbf{f}^a) \quad (11)$$

The field incident on the detector, $\tilde{U}_D(\mathbf{f})$ is

$$\tilde{U}_D\left(\frac{\mathbf{f}}{M_2M_3}\right) = \tilde{U}_j(\mathbf{f})P(\mathbf{f})Q^{\bar{\nu}\mathrm{NA}_{C_2 out}}_{\bar{\nu}\mathrm{NA}_{C_D in}}(\mathbf{f}) \times Q^{\bar{\nu}M_2M_3\mathrm{NA}_{C_D out}}_{\bar{\nu}M_2M_3\mathrm{NA}_{C_D in}}(\mathbf{f}) \quad (12)$$

If we define the net magnification from the cassegrains C_2 and C_3 as $M = M_2M_3$ then eq. 12 becomes

$$\tilde{U}_D(\mathbf{f}) = \tilde{U}_j(M\mathbf{f})P(M\mathbf{f})Q^{\bar{\nu}\mathrm{NA}_{C_2 out}/M}_{\bar{\nu}\mathrm{NA}_{C_2 in}/M}(\mathbf{f}) \times Q^{\bar{\nu}\mathrm{NA}_{C_D out}}_{\bar{\nu}\mathrm{NA}_{C_D in}}(\mathbf{f}) \quad (13)$$

The above expression is true for any arbitrary, spatially heterogeneous sample which has no restriction on its constituent spatial frequencies. Note that M is typically larger than 1 (i.e. the detector elements are bigger than the corresponding areas on the sample).

2.2. Analysis

An analysis of the equations for the FT-IR imaging system provides important insights into optical design and image formation. From Eqn.13 we observe that

$$|\mathbf{f}| \leq \min(\bar{\nu}\mathrm{NA}_{C_2 out}/M, \bar{\nu}\mathrm{NA}_{C_D out}) \quad (14)$$

due to the $Q^{\bar{\nu}\mathrm{NA}_{C_2 out}/M}_{\bar{\nu}\mathrm{NA}_{C_D in}/M}(\mathbf{f})$ and $Q^{\bar{\nu}\mathrm{NA}_{C_D out}}_{\bar{\nu}\mathrm{NA}_{C_D in}}(\mathbf{f})$ terms. When the pre-optics to the detector are well designed, then

$$\bar{\nu}\mathrm{NA}_{C_2 out}/M < \bar{\nu}\mathrm{NA}_{C_D out} \quad (15)$$

Consequently, the limiting field on the detector is a spatial frequency of $\bar{\nu}\mathrm{NA}_{C_2out}/M$. The detector measures field intensity rather than the field itself [5]. The intensity $I(\mathbf{r}) = E^*(\mathbf{r})E(\mathbf{r})$ has twice the spatial frequency bound i.e. $2 \times \bar{\nu}\mathrm{NA}_{C_2out}/M$. In order to faithfully record the entire intensity image without any loss of information, the sampling rate according to Nyquist criterion [5] has to be at least twice this limiting frequency or $4\bar{\nu}\mathrm{NA}_{C_2out}/M$. The pixel size, which is inversely related to the sampling rate is given by $L_{pixel} = M/(4\bar{\nu}\mathrm{NA}_{C_2out})$. We note that the value of spatial sampling rate calculated above is *not* the same as resolution (i.e. Rayleigh criterion [5]), but is the least sampling rate required to preserve all the information obtainable from FT-IR spectroscopic imaging.

The wavenumber, $\bar{\nu}$, in mid-infrared spectroscopic imaging typically varies between $600cm^{-1}$ and $4000cm^{-1}$. In measurements involving human tissues, there is typically little or no information between $3400cm^{-1}$ and $4000cm^{-1}$ and therefore, it is sufficient to optimize our design for $\bar{\nu} = 3400cm^{-1}$. The equivalent pixel size on the sample, therefore, has to be $1/(4 \times 0.34\mathrm{NA}_{C_2out})\mu m$. Thus, for a $\mathrm{NA}_{C_2out} = 0.45$, the effective pixel size on the sample is $1.63\mu m$ and for $\mathrm{NA}_{C_2out} = 0.65$, the effective pixel size is $1.13\mu m$. In current commercial instruments, the pixel size is typically $5.5\mu m$ or $6.25\mu m$, which is significantly larger than optimal for the provided objective (NA $\cong$ 0.45). Our model has shown that it is possible to obtain higher image quality from current instruments by reducing the pixel size. We observe from the model that one avenue for changing effective pixel size is by increasing the magnification (M) between the sample and the detector. This is achieved experimentally by replacing Cassegrain C_2 (15X magnification) by one with 74X magnification. This new Cassegrain also has an NA of 0.65 as opposed to 0.45 on the older Cassegrain. Such a Cassegrain gives an effective pixel size of $1.1\mu m$ on the sample and meets our design criteria. In the following sections, the benefits of improved image quality from the new design are leveraged in breast tissue classification. We demonstrate that previously inaccessible chemical and morphological information have now become available for improved diagnosis.

3. TISSUE CLASSIFICATION

We perform tissue classification by adapting methods proposed by Fernandez et al. [7] for FT-IR images of prostate biopsies. We limit our classifier to two tissue types in order to clearly demonstrate the advantages if our proposed modifications to commercially available imaging systems. We focus on the identification of epithelium and stroma cell types, since these are important for the diagnosis of breast cancer in 2D tissue biopsy samples.

A set of spectral features is first manually identified by an experienced spectroscopist. These features are selected based on chemical characteristics of the relevant cell types and are based on average spectra from pixels identified as epithelium and stroma. The resulting measurements are compiled into a feature vector of 144 measurements. We then construct training and test data by labeling pixels in infrared images of two independent tissue micro-arrays (TMAs). Pixel labeling is performed by an experienced pathologist based on the histology of neighboring tissue sections (Fig. 2), stained with hematoxylin and eosin (H&E) and various immunostains specifically designed for the identification of stromal and epithelial cells.

This provides training data consisting of spectral feature vectors and corresponding class labels. This data set is used to train a Naive Bayesian classifier to determine the posterior probability of a class given a set of features: $P(C|V_0, ..., V_n)$. This Naive Bayesian model is then used to perform automated classification of the training image. In order to prevent overfitting due to a large feature set (in our case 144 features), we identify a subset of features using a greedy approach. We first select the single feature that provides the best classifier performance and iteratively add features until classifier performance on the validation data converges.

This classifier is then used to segment the test image and performance is determined using the reciever operating characteristic (ROC) curve, which plots classifier sensitivity against specificity. The posterior probability of class C_0 is used as a threshold value to determine specificity. Classifier performance is quantified by computing the area under the ROC curve, where a value of 1.0 indicates a perfect classifier and a value of 0.5 indicates random classification (a coin flip). For a given feature vector, this value also identifies the probability of a pixel of class C_0 having a higher posterior value than a pixel of class C_1.

4. RESULTS AND DISCUSSION

Based on the optimal design in Section 2.2 modify an existing infrared spectroscopic imaging system to collect data at this sampling rate and show that the additional resolution at higher wavenumbers can be used to improve the identification of epithelial cells in breast tissue samples.

The training and validation sets are composed of two separate tissue microarrays (TMAs) purchased from Biomax Inc. (www.biomax.us). Two adjacent tissue sections are collected for IR imaging and histology. Imaging was performed using two systems: (a) a Perkin-Elmer Spotlight 300 Imaging system with a 15X (0.45NA) objective with a $6.25\mu m$ pixel size, and (b) a custom-modified Agilent Technologies Varian 7000 Interferometer and 620-IR microscope with a 74X objective (0.65NA) and a $1.1\mu m$ pixel size.

A histologist labeled pixels in the 15X mid-infrared images to identify epithelial and stromal cells. These cell types were selected because they are the most helpful for cancer diagnosis. The Naive Bayesian classifier was then tuned to

identify a set of 33 features. The area under the ROC curve for the identification of epithelial cells is approximately 0.991.

This classifier was then applied to both the 15X and 74X images of the validation array (Fig. 2). The most striking difference is in the labeling of individual lobules composing terminal ductal lobular units (TDLUs). In normal tissue samples, TDLUs are separated by a thin layer of intra-lobular stroma (ILS). In the 15X image, the lobules are merged together, particularly in the lower-left region of the tissue core. This makes the identification of a breast tumor ambiguous. The merged TDLUs can be a result of either excessive growth of epithelial cells, as is the case in a malignant breast tumor, or low chemical resolution due to sampling. In the 74X image, note that the TDLUs are clearly differentiated and ILS is properly labeled.

In this paper, we describe a rigorous model for characterizing infrared light propagation through a spectroscopic imaging system. This model is then used to identify the sampling rate required for optimal resolution of chemical species in a spatially resolved specimen. It is important to note that current instruments, while providing high NA, do not have the correct pixel size to utilize the high NA. These results indicate that current FT-IR imaging systems can be further optimized to achieve significantly greater chemical resolution. With the introduction of optimally designed high-resolution systems, mid-infrared spectroscopic imaging is a promising alternative to current histological methods since it provides quantitative data that can be used to automatically identify tissue type.

Promising future directions for this work include the implementation of multi-class segmentation algorithms. Since spectroscopic imaging is quantitative, the resulting classified images may provide more accurate results when used for automated pathology, which currently rely on chemical staining and imaging with visible light [8].

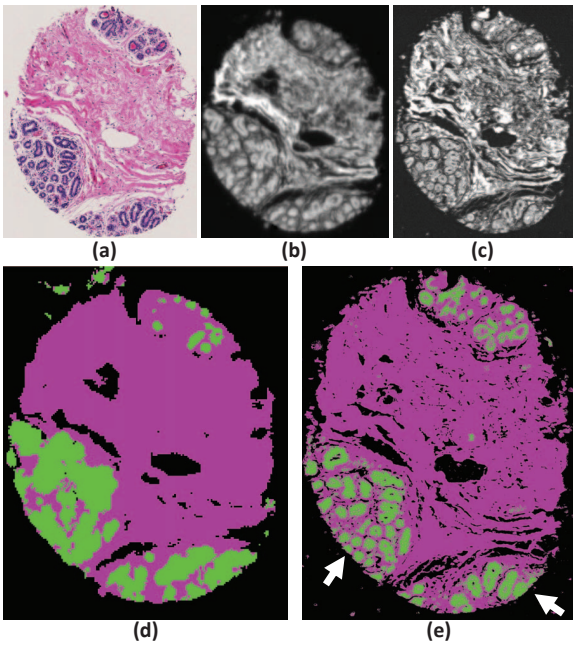


Fig. 2. A TMA breast core imaged using a commercial system at 15X and our proposed 74X method. (a) The H&E histology of a neighboring section is used to identify epithelial cells in the core. Infrared absorbance at $1650cm^{-1}$ is shown for both the 15X (b) and 74X (c) objectives. The final classified images are shown for 15X (d) and 74X (e). Note that individual TDLUs are merged in the 15X image, forming a large region of epithelium that can easily be misclassified as a tumor. Clear separation of TDLUs is seen in the 74X image (arrows).

5. REFERENCES

[1] C.D. Craver, "The coblentz society desk book of infrared spectra," Tech. Rep., DTIC Document, 1977.

[2] E.N. Lewis, P.J. Treado, R.C. Reeder, G.M. Story, A.E. Dowrey, C. Marcott, and I.W. Levin, "Fourier Transform Spectroscopic Imaging Using an Infrared Focal-Plane Array Detector," *Anal. Chem.*, vol. 67, no. 19, pp. 3377–3381, 1995.

[3] P.R. Griffiths and J.A. De Haseth, *Fourier Transform Infrared Spectroscopy*, John Wiley & Sons, 1986.

[4] R. Reddy, B. Davis, P.S. Carney, and R. Bhargava, "Modeling fourier transform infrared spectroscopic imaging of prostate and breast cancer tissue specimens," *IEEE International Symposium on Biomedical Imaging*, pp. 738–741, 2011.

[5] J.W. Goodman, *Introduction to Fourier Optics*, Roberts & Company Publishers, 2005.

[6] P.A.M. Dirac, *The Principles of Quantum Mechanics*, Oxford University Press, 1958.

[7] D.C. Fernandez, R. Bhargava, S.M. Hewitt, and I.W. Levin, "Infrared spectroscopic imaging for histopathologic recognition," *Nat. Biotechnol.*, vol. 23, no. 4, pp. 469–474, 2005.

[8] A.H. Beck, A.R. Sangoi, S. Leung, R.J. Marinelli, T.O. Nielsen, M.J. van de Vijver, R.B. West, M. van de Rijn, and D. Koller, "Systematic analysis of breast cancer morphology uncovers stromal features associated with survival," *Science Translational Medicine*, vol. 3, no. 108, pp. 108–113, 2011.